View metadata, citation and similar papers at core.ac.uk

brought to you by CORE

provided by Elsevier - Publisher Connector

NEOPLASIA
www.neoplasia.com

Volume 17 Number 2 February 2015 pp. 208–214 208

Pushing the Optical Imaging Limits of Cancer with Multi-Frequency-Band Raster-Scan Optoacoustic Mesoscopy (RSOM)

Murad Omar[1], Mathias Schwarz[1], Dominik Soliman, Panagiotis Symvoulidis and Vasilis Ntziachristos

Biological Imaging, Technische Universitaet Muenchen, Ismaningerstr. 22, 81675, Muenchen, Germany; Institute for Biological and Medical Imaging, Helmholtz Zentrum Muenchen, 85764, Neuherberg, Germany

Abstract

Angiogenesis is a central cancer hallmark, necessary for supporting tumor growth and metastasis. *In vivo* imaging of angiogenesis is commonly applied, to understand dynamic processes in cancer development and treatment strategies. However, most radiological modalities today assess angiogenesis based on indirect mechanisms, such as the rate of contrast enhancement after contrast agent administration. We studied the performance of raster-scan optoacoustic mesoscopy (RSOM), to directly reveal the vascular network supporting melanoma growth *in vivo,* at 50 MHz and 100 MHz, through several millimeters of tumor depth. After comparing the performance at each frequency, we recorded, for the first time, high-resolution images of melanin tumor vasculature development *in vivo,* over a period of several days. Image validation was provided by means of cryo-slice sections of the same tumor after sacrificing the mice. We show how optoacoustic (photoacoustic) mesoscopy reveals a potentially powerful look into tumor angiogenesis, with properties and features that are markedly different than other radiological modalities. This will facilitate a better understanding of tumor's angiogenesis, and the evaluation of treatment strategies.

Neoplasia (2015) 17, 208–214

Introduction

Imaging of tumor growth, tumor dynamics, and tumor angiogenesis is important in elucidating tumor biology and physiology [1,2], and understanding the tumor microenvironment [3,4]. Tomographic systems, such as positron emission tomography (PET) [5], magnetic resonance imaging (MRI) [6], or fluorescence molecular tomography (FMT) [7], have been employed to resolve vasculature and angiogenesis. However, these modalities do not directly resolve the vascular bed. PET and FMT reveal vasculature based on contrast-enhanced low resolution images. The enhancement is achieved by blood-pool agents, essentially radio-isotopes or fluorochromes that are restrained in the vascular system. Optical tomography methods can in principle, directly resolve the absorption of blood vessels, without the need for contrast agents; however, the low resolution achieved, and the mixed contributions of absorption and scatter, deterred its wide-use for imaging angiogenesis. The resolution of these systems does not exceed 1 mm, even when small animals are considered. Therefore only bulk measures of the vascular bed are assessed.

MRI offers higher resolution, but similarly to other radiological methods, does not directly resolve the vasculature. Instead, angiogenesis can be indirectly assessed through arterial spin labeling (ASL), or blood oxygenation level-dependent (BOLD) [8]. Dynamic contrast-enhanced (DCE)-MRI is considered as a more direct method for measuring angiogenesis [8–10], but it generally visualizes bulk effects present after enhancement by a contrast agent and not individual small vessels. To image smaller vessels, micro-MRI could be used [11], but it is so far better suited for *ex-vivo* studies. Similarly, ultrasound imaging is not sensitive in visualizing small blood vessels. Contrast enhanced volumetric X-ray CT (VCT) has been also considered for vasculature imaging, yielding visualization of blood

Address all correspondence to: Vasilis Ntziachristos, Chair for Biological Imaging, Technische Universitaet Muenchen, Ismaningerstr. 22, 81675, Muenchen, Germany. E-mail: v.ntziachristos@tum.de

[1]These authors contributed equally to this work.

Received 29 October 2014; Revised 19 December 2014; Accepted 23 December 2014

© 2015 Neoplasia Press, Inc. Published by Elsevier Inc. This is an open access article under the CC BY-NC-ND license (http://creativecommons.org/licenses/by-nc-nd/4.0/).

1476-5586/15
http://dx.doi.org/10.1016/j.neo.2014.12.010

vessels with diameters as small as 50 μm after contrast enhancement [12]. Complication of this technique include the use of ionizing radiation, and the administration of contrast agents which are not well tolerated in longitudinal studies [13].

While bulk measures of angiogenesis offer useful insights in assessing anti-angiogenic treatment, the ability to visualize at higher resolution is a sought after target as it allows a better insight into the architecture, and the dynamic evolution of the vascular network supporting tumor growth and metastasis. Images of individual venules and arterioles can be achieved by optical microscopy techniques, such as multiphoton microscopy [14], applied *in-vivo*. Intravital microscopy has enabled high-resolution angiogenesis insights [2], revealing important details on the structural and functional alterations of blood vessels, better explaining the tumor micro-environment and the successes or failures of different treatment strategies. Optoacoustic (photoacoustic) microscopy has also demonstrated potential for imaging vasculature in high-resolution and *in-vivo*[15,16]. The natural label-free contrast mechanism of optoacoustic methods is the absorption of light. As hemoglobin is a major absorber of light in the visible, and the near-infrared regions, blood vessels, containing concentrated hemoglobin, can be accurately resolved by optoacoustic methods [17]. However, the caveat of optical microscopy methods is that only a small fraction of the tumor is typically visualized [18,19]. While mosaicking techniques are available to reveal a larger field of view, it is not possible to penetrate highly scattering tissues, such as malignant tumors and surrounding tissues, much deeper than a few hundred microns. Therefore the information obtained with these methods, is only a partial picture of the tumor environment. Moreover, many intravital approaches require an optical window, surgically placed on the tumor; an invasive procedure, which also provides a partial view of the tumor microenvironment [20]. Optical coherence tomography, implemented in the frequency domain, has been also employed for imaging vasculature in the tumor microenvironment [21], but it was capable of imaging vessels up to a depth of only ~ 1 mm so far.

Even though optoacoustic microscopy based on optical focusing, is limited by depth, optoacoustic signals based on ultrasound focusing, are highly scalable and enable penetration through several millimeters to centimeters of tissue. In this case, resolution can be exchanged with penetration depth; i.e. the higher the resolution the more superficial the imaging. Although a precise relationship between resolution and depth is difficult to establish, as it depends on multiple system and tissue parameters, optoacoustic imaging at frequencies on the order of 20 to 30 MHz have achieved resolutions of 70 to 100 μm [22]. In these images, only large vessels of minimum apparent diameter of 81 μm have been observed [22].

In this work we showcase how an emerging optoacoustic implementation termed raster-scan optoacoustic mesoscopy (RSOM), can be employed to break through the limits of current methods of tumor angiogenesis imaging, and provide high-resolution optoacoustic mesoscopy of tumor vasculature. We investigate how frequency and band, affect the imaging ability by implementing RSOM at 50 MHz central frequency (RSOM 50), and 100 MHz central frequency (RSOM 100). Both these implementations lead to ultra-wide band measurements, for example the RSOM100 implementation has an ultrasound frequency bandwidth of approximately 160 MHz. This presents a unique inversion problem, which is addressed herein using a novel frequency-dependent inversion, shown necessary for optimally accommodating the broad bandwidth of the measurements. This technological progress leads to new, previously not reported, performance in resolving tumor vasculature reaching better than 5 μm axial resolution, and better than 20 μm lateral resolution through at least 3 mm of tissue depth. We discuss the implications of these new features in better understanding tumor angiogenesis at the entire tumor level

Materials and Methods

Imaging studies were based on a home built RSOM system, previously described by Omar et al. [23,24]. In epi-illumination mode, the technique has yielded 4 μm axial and 18 μm lateral resolution in tissue mimicking phantoms, through several millimeters of depth [24]. Figure 1 shows the system, which is based on spherically focused, high-frequency ultrasound detectors, with both 50 MHz, and 100 MHz central frequency. The 50 MHz detector has an active aperture diameter of 3 mm, an f-number of 0.99, and a bandwidth of 10 to 90 MHz, while the 100 MHz detector has an active aperture of 1.5 mm, an f-number of 1.1, and a bandwidth of 20 to 180 MHz. The excitation is based on a fast, nano-second laser, operating at 532 nm, and with a pulse repetition frequency of 2 kHz (Wedge HB532, Bright Solutions SRL, Pavia, Italy). The measured signals are amplified by a low noise amplifier with a gain of 63 dB (AU-1291, Miteq Inc., USA), and subsequently acquired with a sampling frequency of 1 GSps (EON-121-G20, Gage-applied, Montreal, Canada). The raster-scanning is performed in a continuous-discrete manner to expedite the measurements; the step sizes are 8 μm for RSOM100 and 15 μm for RSOM50 [23,24].

To examine the capacity of the system in resolving tumor angiogenesis, B16F10 melanoma cells (0.5×10^6 cells in 25 μl PBS solution) were injected subcutaneously into the mammary fat pad of four 8 weeks old female Hsd:Athymic Nude-Foxn1^{nu} mice. Melanoma tumor growth and vascular changes were monitored over a time course of 8-9 days. Each animal was scanned up to three times, with an additional final scan directly before euthanasia.

For the *in vivo* experiments, a custom-made mouse bed was designed, shown in Figure 1*A*. The bed was slightly curved, increasing in height towards the headpiece, to keep the animal's head above water. During the experiment the mice lay on their back with a boundary on the sides of the bed to hold them in position. The ROI around the tumor side was covered by a thin plate, made of acrylic glass, with a 2 × 2 cm opening in the center. The opening was sealed with a thin plastic membrane and coupled to the mouse skin above the ROI with ultrasound gel. The mouse bed was immersed in warm water, covering the ROI by several millimeters and the body temperature was maintained at 36°C. The mice were imaged under 1.8% isoflurane anesthesia. All procedures were approved by the District Government of Upper Bavaria.

For reconstruction, three-dimensional beamforming with a dynamic aperture was used [23,24]. Because of the ultra-wide bandwidth of the employed detectors, we divided the reception bandwidth into several smaller sub-bands [24,25]. In this way, images are reconstructed using a sequential narrow band inversion (SNBI), which inverts the low frequencies separately from the high frequencies. In this work a 2-band split was performed; however, a finer band reconstruction can be implemented. The advantage of SNBI is that each frequency band is reconstructed with parameters better suited to the signal-to-noise characteristics of the band. By also rendering the different bands reconstructed in different colors [24], on the same final image, the resulting image allows for a better

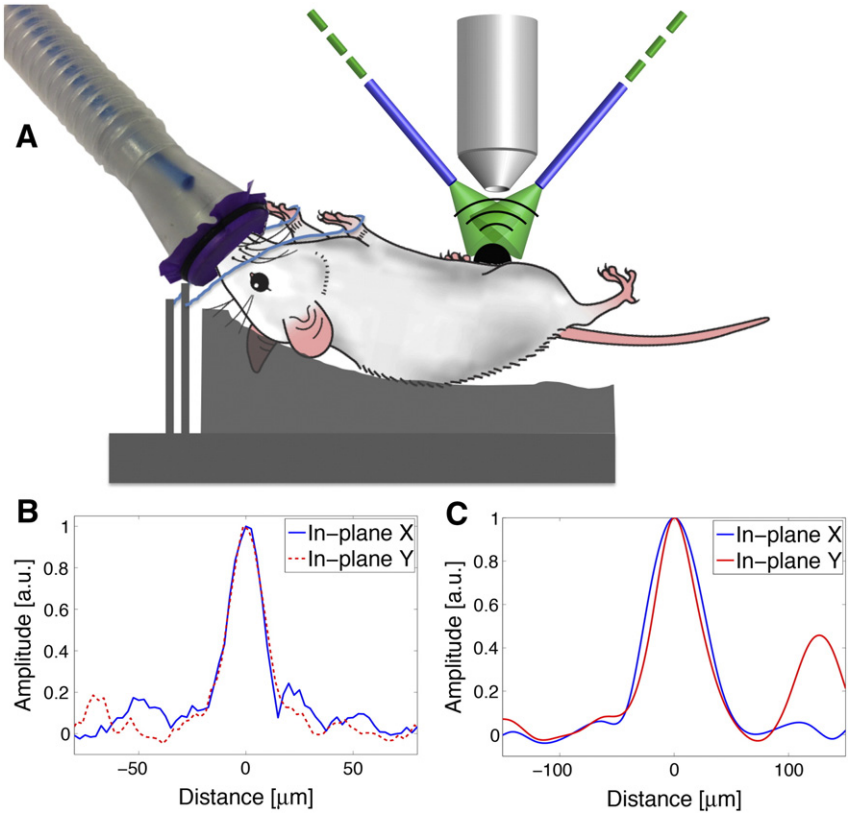

Figure 1. (A) Depiction of the raster scan system, showing the position of the mouse, the mouse bed, anaesthesia, the detector, and the illumination, (B) depiction of the two lateral profiles through a 3 μm sphere, characterizing the resolution of RSOM100, and (C) profiles through a 10 μm sphere characterizing resolution of RSOM50.

representation of the high frequencies (smaller structures) avoiding their masking by the low frequencies on the final reconstruction. To assure that no ringing effects appear from filtering, we divided the frequencies in such a way, that the relative bandwidth was kept constant for all the sub-bands:

$$\frac{BW_1}{f_{c1}} = \frac{BW_2}{f_{c2}} = \frac{BW_3}{f_{c3}} = \dots$$

In case of the 100 MHz detector, we divided the reception bandwidth into 2 sub-bands with 100% relative bandwidth, a similar procedure was applied to the 50 MHz detector. After choosing the value of the relative bandwidths, and the first cutoff frequency, the next cutoff frequency could be determined as:

$$f_2 = \frac{2 + BW_{\%}}{2 - BW_{\%}} f_1.$$

Throughout this work, we applied a color map where red represents the reconstruction of the low frequencies, 20 to 60 MHz for RSOM100, and 10 to 30 MHz for RSOM50, and green represents high frequencies, 60 to 180 MHz for RSOM100 and 30 to 90 MHz for RSOM50.

For validation purposes we used our prototype imaging cryo-microtome [26,27]. Reflection (RGB), and Fluorescence (740/780 exc/emm wavelengths) imaging were acquired resulting in a multispectral volume with voxel dimensions of ~ 25 × 25 × 50 µm.

Results and Discussion

To compare the performance of the two different detectors, we show in Figure 1, *B* and *C* lateral profiles through a 3 µm sphere for RSOM100, and through a 10 µm sphere for RSOM50 (both are polybead black dyed microspheres, Polysciences Inc., Warrington, PA, USA), the calculated full width at half maximum (FWHM) of the profiles is 18 µm, and 45 µm respectively.

Figure 2, *A* and *B*, shows a zoom into a vascular network recorded with the two systems. In Figure 2*C*, a profile of the vessels marked by the arrow in Figure 2, *A* and *B*, is shown and the FWHM is calculated. With RSOM50 and RSOM100, we obtain lateral resolutions of 42.5 µm and 20 µm, respectively, which corresponds well to the characterization using the microspheres in Figure 1.

For direct comparison of the two different detectors, we show in Figure 2, *D* and *E* the same ROI at Day 4 after melanoma cell injection acquired with the 100 MHz and the 50 MHz detector. Figure 2, *D* and *E* shows a black hole where the tumor is located. The vasculature around the tumor can be clearly identified, however showing some discontinuities, which could be attributed, to the higher f-number, and thus the lower angle of acceptance, of the 100 MHz detector. Thus, long tilted structures, such as vessels, which generate an optoacoustic wave normal to them, i.e. oblique to the axis of the detector will not be detected. In Figure 2*E*, we clearly observe an improved image quality, where vessels appear as continuous structures, the appearance of additional vasculature in Figure 2*E* compared to Figure 2*D* is attributed, to the best of our knowledge, to the lower f-number, i.e. higher angle of acceptance, of the 50 MHz detector, thus even some of the tilted vasculature could be observed.

In Figure 3, tumor growth over time is followed, the images were measured using RSOM50. For better visualization, a partial MIP of the reconstruction is taken, where instead of taking the MIP of the whole volume we rather start at a depth of ~ 900 µm below the surface

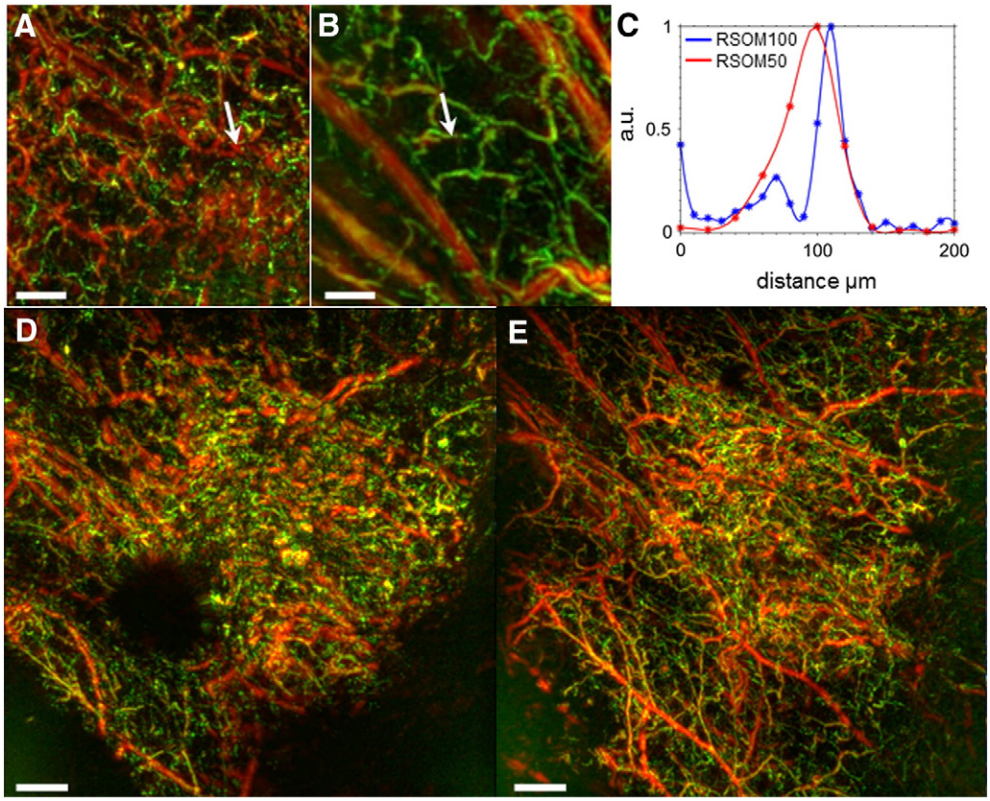

Figure 2. Comparison of the imaging performance achieved by RSOM100 and RSOM50 imaging the vasculature of a melanoma tumor. An ROI of 3 mm × 3 mm was acquired with A) RSOM100, and B) RSOM50. C) Lateral profile through the vessels marked by the green arrow in A and B). D and E) MIPs of the same ROI around the tumor at Day 4 after tumor cell injection. D) In RSOM100, the center of the tumor shows up as a black hole. E) In RSOM50, the vasculature appears as a continuous network. (Scale bars: A and B: 500 μm, d and e: 1 mm).

of the skin, this way both tumor's growth and the re-arrangement of the vessels around the tumor, as well as the growth of new vessels due to angiogenesis, are observed on the same image. Additionally, the inset in every subfigure of Figure 3 shows a zoom-in on the same area, through all the days, from a location in the proximity of the tumor. From the sub-figures the growth of the tumor, represented by the growth of the black non-vascularized spot, indicated by a thick arrow, is observed. Additionally, in the inset it is observed that upon interaction with the tumor, the two big vessels, a thick arrow points to that region, start re-arranging, while at the same time, smaller vessels start growing in that region. Due to tumor growth, the flexibility of skin and differences in fixing the tumor location through the different days, it is not possible to show the exact same ROI in all the subfigures of Figure 3.

Figure 4 shows a volumetric representation of a tumor imaged at Day 9, which was validated by cryo-slices. In Figure 4(a), a maximum intensity projection (MIP) of the ROI from 930 µm to a depth of 2115 µm away from the focus is shown. The tumor itself shows up as a dark area, because the melanin-rich tumor strongly absorbs visible laser light already in the upper layers, and high-frequency detectors cannot detect the extremely low frequencies generated from the tumor bulk, on the order of 0.1 to 1 MHz. Figure 4*A* correlates well with the cryo-slice taken at a depth of 930 µm, as shown in Figure 4*E*. In Figure 4, *B*–*D*, a MIP of the ROI from 615 µm, 390 µm, 0 µm to a depth of 2115 µm are shown, visualizing the feeding vessels of the tumor. Figure 4, *B* and *C* correlate well to the corresponding cryo-slices shown in Figure 4, *F* and *G*Figure 4*H* shows a volumetric image of the ROI. The tumor appears as a bump on this image, with vasculature surrounding it.

Conclusions

We demonstrated imaging of tumor growth, the corresponding arrangement of the surrounding vascular network, and the growth of new micro-vasculature in the vicinity of the tumor using ultra-wideband raster-scan optoacoustic mesoscopy (RSOM). To the best of our knowledge, this is the first time that tumor vasculature is imaged at such depths with such resolution *in-vivo*. We showed that RSOM could be applied longitudinally and resolve growth-related changes of the same tumor.

In this work, we compared the performance of RSOM implementation at 50 MHz and 100 MHz. The images obtained show that imaging using the 100 MHz detector results to measurable improvements in image ability by resolving smaller structures, such as the newly sprouting vessels, especially when implemented with multi-frequency reconstruction, so that the high frequencies are not masked by low frequencies [24,25]. On the other hand, as expected, the 50 MHz detector performs better in imaging larger structures generating lower frequencies, such as large blood vessels (larger than 50 µm in diameter), thus most of the vasculature are better seen with the 50 MHz detector. Additionally, the smaller f-number (i.e. higher angular coverage) of the 50 MHz detector performs better in imaging oblique vessels, thus the vasculature appears more continuous in RSOM50

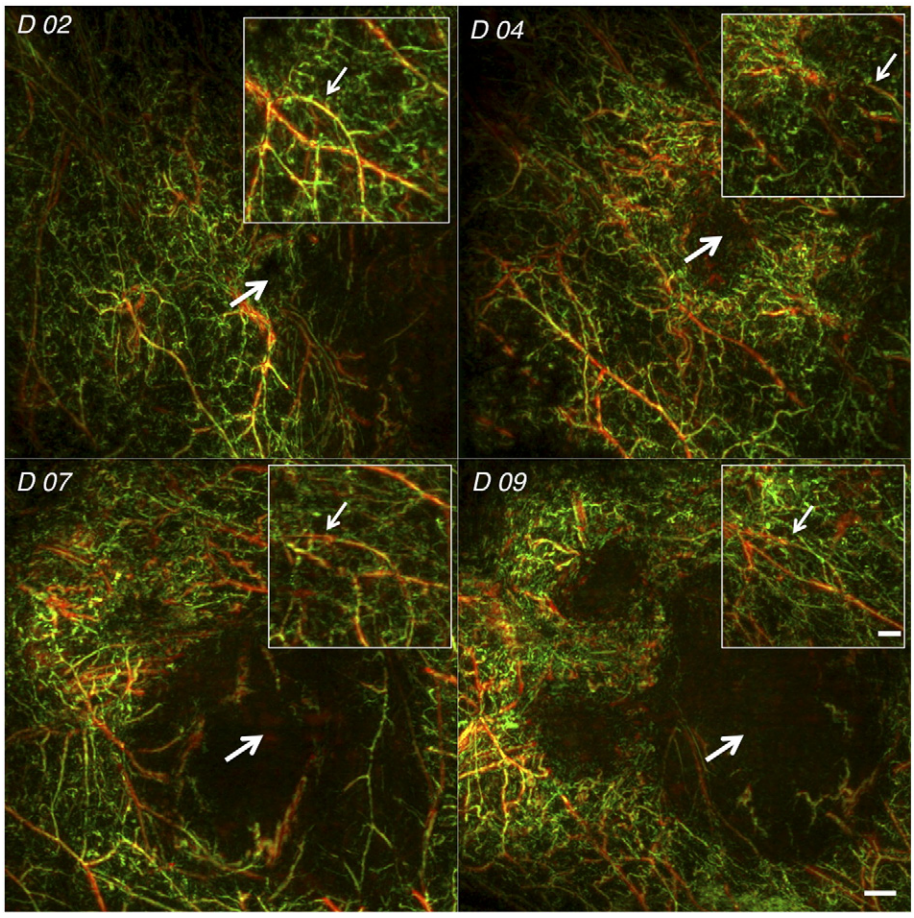

Figure 3. Tumor growth over time. Images of the tumor area were acquired at Day 2, Day 4, Day 7, and Day 9 after injection of the melanoma cells, the thick arrow points to the tumor. The images are generated by taking the maximum intensity projection of the tumor from a depth of 900 μm from the surface of the tumor. The inset in every image, shows the same region, from an area very close to the tumor, and shows two large vessels (the arrow points to that region), between which small vessels grow over time. (Scale bar: 1 mm in the images, 0.5 mm in the inset.)

images compared to RSOM100 images, and some of the vasculature that do not appear with the 100 MHz detector, could be more efficiently measured with the 50 MHz detector, as seen in Figure 2. Because of this, the data from RSOM100 could be used in a hybrid implementation together with RSOM50 to offer a more complete picture of the tumor micro-vasculature. RSOM100 could be used to image the tumor in the first days of development, or image the small sprouting micro-vessels, and RSOM50 could provide complementary information especially as tumor structures and vessels become larger as a function of tumor growth. In this case image processing, and image co-registration tools could be employed to merge together the images collected at the different spectral bands.

Applying multi-frequency reconstruction improves the visibility of the small structures, i.e. structures corresponding to high frequencies, such as the newly sprouting vessels during angiogenesis. Because the amplitude of the signals is proportional to the size of the object generating those signals, the high-frequencies generally have a lower *SNR* compared to the low frequencies. Additionally high-frequencies are more strongly attenuated than low frequencies, thus if all the frequencies are simultaneously reconstructed, the high-frequencies will be masked by the low frequencies. By processing the high-frequencies separately, it is possible to process them better, and subsequently improve the visibility for small structures [24].

The obtained capabilities should enable a better understanding of tumor growth, and tumor angiogenesis, which is important in understanding tumor's physiology, mechanisms of metastasis, and planning of therapy, where RSOM is capable of imaging tumor's growth, tumor's angiogenesis, and theoretically tumor's response to various kinds of therapy. This specifically applies to those kinds of therapies that affect tumor vasculature, target tumor angiogenesis, and which are based on enhanced permeability and retention (EPR) [3,4]. This could be applied not only to pre-clinical research, but also in clinical environments, such as skin imaging [25].

Finally, further technological advances, such as advances in laser technology, illumination configuration [28], and detection technology, would enable better imaging capabilities for RSOM. For instance by using additional laser lines in RSOM, not only anatomical images could be generated, but also functional images visualizing tumor metabolism, oxygenation maps and hypoxia regions inside the tumor could be obtained. Additionally, applying smart algorithms to this multispectral data will improve the detection sensitivity [29]. Using point ultrasonic detectors, (e.g. waveguide Bragg grating (WBG) [30]) with a broad, flat bandwidth will improve the detection of lower and higher frequencies, as well as the angular coverage of the detector, and thus enable miniaturization of the system, and multi-scale imaging.

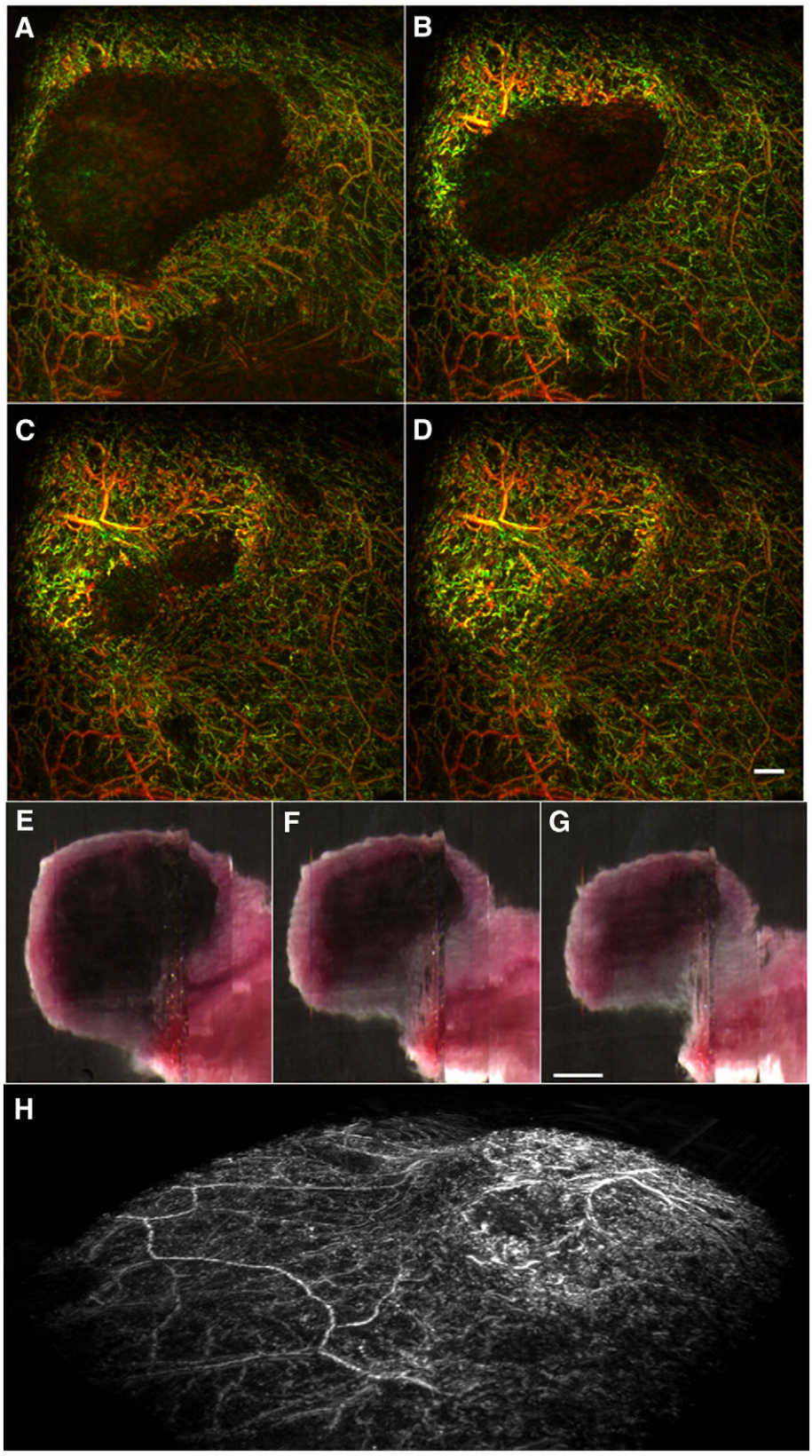

Figure 4. Volumetric representation of RSOM data, taken at Day 9 post injection, and correlation with cryo-slices the same tumor. MIP of the volumetric RSOM data from a depth of A) 930 μm, B) 615 μm, C) 390 μm, and D) 0 μm to a depth of 2115 μm. E–G) correspondingly show cryo-slices taken at a depth of 930 μm (E), 615 μm (F), and 390 μm (G). H) 3D visualization of the whole ROI. Arrows point to the location of the tumor. Scale bar: (D) 1 mm, (G) 2 mm.

Acknowledgements

The authors would like to thank Dr. Angelika Zaremba for preparing the animals protocol, the authors would like also to thank Uwe Klemm, Sarah Glasl, and Florian Jurgeleit for help with animal handling. VN acknowledges financial support from the ERC Advanced Grant "Next Generation in-vivo imaging platform for post-genome biology and medicine MSOT" (233161), and the DFG Reinhart Koselleck project "High resolution near-field thermoacoustic sensing and imaging" (NT 3/9-1).

References

[1] Hanahan D and Weinberg RA (2011). Hallmarks of cancer: the next generation. *Cell* **144**, 646–674.
[2] Carmeliet P and Jain RK (2000). Angiogenesis in cancer and other diseases. *Nature* **407**, 249–257.
[3] Lammers T, Kiessling F, Hennink WE, and Storm G (2012). Drug targeting to tumors: principles, pitfalls and (pre-) clinical progress. *J Control Release* **161**, 175–187.
[4] Maeda H (2012). Macromolecular therapeutics in cancer treatment: the EPR effect and beyond. *J Control Release* **164**, 138–144.
[5] Gambhir SS (2002). Molecular imaging of cancer with positron emission tomography. *Nat Rev Cancer* **2**, 683–693.
[6] Charles-Edwards EM (2006). Diffusion-weighted magnetic resonance imaging and its application to cancer. *Cancer Imaging* **6**, 135.
[7] Ale A, Ermolayev V, Herzog E, Cohrs C, de Angelis MH, and Ntziachristos V (2012). FMT-XCT: in vivo animal studies with hybrid fluorescence molecular tomography-X-ray computed tomography. *Nat Methods* **9**, 615–620.
[8] Barrett T, Brechbiel M, Bernardo M, and Choyke PL (2007). MRI of tumor angiogenesis. *J Magn Reson Imaging* **26**, 235–249.
[9] Oto A, Yang C, Kayhan A, Tretiakova M, Antic T, Schmid-Tannwald C, Eggener S, Karczmar GS, and Stadler WM (2011). Diffusion-weighted and dynamic contrast-enhanced MRI of prostate cancer: correlation of quantitative MR parameters with Gleason score and tumor angiogenesis. *Am J Roentgenol* **197**, 1382–1390.
[10] O'Connor JP, Jackson A, Parker GJ, and Jayson GC (2007). DCE-MRI biomarkers in the clinical evaluation of antiangiogenic and vascular disrupting agents. *Br J Cancer* **96**, 189–195.
[11] Kim E, Zhang J, Hong K, Benoit NE, and Pathak AP (2011). Vascular phenotyping of brain tumors using magnetic resonance microscopy (μMRI). *J Cereb Blood Flow Metab* **31**, 1623–1636.
[12] Kiessling F, Greschus S, Lichy MP, Bock M, Fink C, Vosseler S, Moll J, Mueller MM, Fusenig NE, and Traupe H, et al (2004). Volumetric computed tomography (VCT): a new technology for noninvasive, high-resolution monitoring of tumor angiogenesis. *Nat Med* **10**, 1133–1138.
[13] Maehara N (2003). Experimental microcomputed tomography study of the 3D microangioarchitecture of tumors. *Eur Radiol* **13**, 1559–1565.
[14] Alexander S, Weigelin B, Winkler F, and Friedl P (2013). Preclinical intravital microscopy of the tumour-stroma interface: invasion, metastasis, and therapy response. *Curr Opin Cell Biol* **25**, 659–671.
[15] Yao J and Wang LV (2013). Photoacoustic microscopy. *Laser Photonics Rev* **7**, 758–778.
[16] Yao J, Maslov KI, Zhang Y, Xia Y, and Wang LV (2011). Label-free oxygen-metabolic photoacoustic microscopy in vivo. *J Biomed Opt* **16** [076003-076003-076011].
[17] Kruger RA, Liu P, Fang Y, and Appledorn CR (1995). Photoacoustic ultrasound (PAUS)-Reconstruction tomography. *Med Phys* **22**.
[18] Tserevelakis GJ, Soliman D, Omar M, and Ntziachristos V (2014). Hybrid Multi-photon and Optoacoustic Microscope. *Opt Lett* **39**.
[19] Ntziachristos V (2010). Going deeper than microscopy: the optical imaging frontier in biology. *Nat Methods* **7**, 603–614.
[20] Kedrin D, Gligorijevic B, Wyckoff J, Verkhusha VV, Condeelis J, Segall JE, and van Rheenen J (2008). Intravital imaging of metastatic behavior through a mammary imaging window. *Nat Methods* **5**, 1019.
[21] Vakoc BJ, Lanning RM, Tyrrell JA, Padera TP, Bartlett LA, Stylianopoulos T, Munn LL, Tearney GJ, Fukumura D, and Jain RK, et al (2009). Three-dimensional microscopy of the tumor microenvironment in vivo using optical frequency domain imaging. *Nat Med* **15**, 1219–1223.
[22] Laufer J, Johnson P, Zhang E, Treeby B, Cox B, Pedley B, and Beard P (2012). In vivo preclinical photoacoustic imaging of tumor vasculature development and therapy. *J Biomed Opt* **17**, 0560161–0560168.
[23] Omar M, Gateau J, and Ntziachristos V (2013). Raster-scan optoacoustic mesoscopy in the 25–125 MHz range. *Opt Lett* **38**, 2472–2474.
[24] Omar M, Soliman D, Gateau J, and Ntziachristos V (2014). Ultrawideband reflection-mode optoacoustic mesoscopy. *Opt Lett* **39**, 3911–3914.
[25] Schwarz M, Omar M, Buehler A, Aguirre J, and Ntziachristos V (2015). Implications of ultrasound frequency in optoacoustic mesoscopy of the skin. *IEEE Trans Med Imaging* **34**(2), 802–824. http://dx.doi.org/10.1109/TMI.2014.2365239.
[26] Sarantopoulos A, Themelis G, and Ntziachristos V (2011). Imaging the bio-distribution of fluorescent probes using multispectral epi-illumination cryoslicing imaging. *Mol Imaging Biol* **13**, 874–885.
[27] Symvoulidis P, Perez CC, Schwaiger M, Ntziachristos V, and Westmeyer G (2014). Serial sectioning and multispectral imaging system for versatile biomedical applications. *Biomedical Imaging (ISBI), 2014 IEEE 11th International Symposium on* 890–893. IEEE; 2014.
[28] Gateau J, Chaigne T, Katz O, Gigan S, and Bossy E (2013). Improving visibility in photoacoustic imaging using dynamic speckle illumination. *Opt Lett* **38**, 5188–5191.
[29] Tzoumas S, Deliolanis N, Morscher S, and Ntziachristos V (2014). Un-mixing Molecular Agents from Absorbing Tissue in Multispectral Optoacoustic Tomography; 2014 .
[30] Rosenthal A, Omar M, Estrada H, Kellnberger S, Razansky D, and Ntziachristos V (2014). Embedded ultrasound sensor in a silicon-on-insulator photonic platform. *Appl Phys Lett* **104**, 021116.